# A Flexible Array Transducer for Photoacoustic-Guided Surgery

Jiaxin Zhang*, Alycen Wiacek*, Eduardo González†, Ziwei Feng*‡, Kai Ding‡, and Muyinatu A. Lediju Bell*†§
*Department of Electrical and Computer Engineering, Johns Hopkins University, Baltimore, MD
†Department of Biomedical Engineering, Johns Hopkins University, Baltimore, MD
‡Department of Radiation Oncology and Molecular Radiation Sciences, Johns Hopkins Medical Institutes, Baltimore, MD
§Department of Computer Science, Johns Hopkins University, Baltimore, MD

***Abstract*—Photoacoustic imaging has recently demonstrated strong viability for surgical guidance, enabling visualization of tool tips during surgery. To receive the photoacoustic signal, most conventional transducers are rigid, while a flexible array is able to deform and provide complete contact on surfaces with different geometries. In this work, we present the first known photoacoustic images acquired with a flexible array transducer in multiple concave shapes targeted toward interventional photoacoustic applications. We provide target depth measurements and quantitative characterization of image quality. The target depth agreement with ground truth ranged 97.28 - 99.24%. The lateral and axial target sizes of a 1 mm diameter target were 1.31 $\pm$ 0.12 mm and 1.70 $\pm$ 0.11 mm, respectively. The mean $\pm$ one standard deviation of target contrast and signal-to-noise ratios were 19.05 $\pm$ 1.47 dB and 61.49 $\pm$ 1.47 dB, respectively. Results establish the feasibility of implementing photoacoustic-guided surgery with a flexible array transducer.**

***Index Terms*—photoacoustic imaging, photoacoustic-guided surgery, flexible array transducers**

## I. Introduction

Photoacoustic imaging has recently demonstrated strong viability for surgical guidance, enabling visualization of tool tips during surgery. In photoacoustic imaging, a tissue region of interest irradiated by the light source, such as the pulsed laser, generates thermal expansion. The produced acoustic waves propagate towards the surface of the tissue and are received by an ultrasound transducer with various time delays [1], [2]. Major features of photoacoustic imaging including high spatial resolution and great penetration depth make it an excellent technique for surgical guidance [3]. However, some of the current surgeries only rely on pre-operative medical images, where the visualization of surgical tools is missing. In such cases, accidental injuries to internal critical structures are possible [4]. To address this challenge, an optical fiber can be inserted inside or appended to the outside of surgical tools needed for an operation (e.g., needle tips [5], catheter tips [6], drill tips needle tips [7], [8]). As signals from both the fiber tip and the tool tip, as well as the region of interest, can be received by the transducer, visualizing tool tips relative to surrounding regions of interest is paper possible [3], [4].

Conventional linear transducers (e.g., clinical hand-held probes, laparoscopic probes) have rigid sensing parts with fixed array geometries, making them ideal for flat surfaces. To receive photoacoustic signals with these transducers placed on uneven surfaces, additional contact pressure is required. This pressure can cause organ distortions, tool tip localization difficulties, possible patient discomfort during interventions that lack anesthesia, and risk of further injury to body tissue [9]. In recent years, the development of advanced sensing technology, such as the flexible array transducer, has provided more opportunities for photoacoustic-guided surgery applications. Instead of the rigid geometry of traditional probes, a flexible array is able to deform and provide complete contact on body parts with different curved surfaces [10], including the skull, spine, and abdomen, which is particularly beneficial for photoacoustic-guided neurosurgery [11], spinal fusion surgery [12], [13], and liver surgery [14]. This type of complete contact minimizes organ deformations, anatomical distortions, and patient discomfort and is expected to improve target localization and visualization.

Major challenges with utilizing the flexible array transducer include array geometry estimation and image reconstruction. To measure transducer element positions, a shape sensing fiber can be attached along the array [15]. Different shape estimation algorithms were proposed, such as updating shape parameters based on image sharpness evaluation [16] or image entropy calculation [17], for ultrasound image formation. For unknown array shapes, deep neural networks were demonstrated as alternatives to generate ultrasound images without distortions [18]. Spinal deformity was also measured by using the flexible array transducer for ultrasound imaging in the phantom study with four known shapes (i.e., flat, convex, concave, and s-shaped) [19]. With respect to photoacoustic signal reception, a flexible Lead Zirconate Titanate (PZT) transducer was fabricated and demonstrated to receive an A-line signal [20]. In addition, Ghavami *et al.* [21] created photoacoustic images with their custom-designed flexible transparent capacitive micromachined ultrasound transducer (CMUT) array in a given curved shape for through-illumination systems.

In this paper, we introduce the first known demonstration of photoacoustic imaging with a flexible array on different curved surfaces for potential interventional applications. We developed mathematical equations for photoacoustic image formation with the flexible array in multiple concave shapes, evaluate on varying surface curvatures and with multiple targets in the same image plane, and characterize the resulting photoacoustic image quality.

2022 IEEE International Ultrasonics Symposium (IUS) | 978-1-6654-6657-8/22/$31.00 ©2022 IEEE | DOI: 10.1109/IUS54386.2022.9957671

Authorized licensed use limited to: Johns Hopkins University. Downloaded on December 27,2022 at 04:18:09 UTC from IEEE Xplore. Restrictions apply.

TABLE I
FLEXIBLE ARRAY TRANSDUCER PARAMETERS

| Parameters | Value |
|---|---|
| Number of Elements | 128 |
| Center Frequency | 5MHz |
| Element Width | 0.8 mm |
| Element Pitch | 1.0 mm |
| Element Height | 10 mm |
| Receive Elements | 128 |

## II. METHODS

### A. Experimental setup

The flexible array transducer (JAR1109, Japan Probe and Hitachi, Japan) was connected to the Vantage 128 System (Verasonics Inc., WA, USA). The parameters of the flexible array transducer are listed in Table 1. A Phocus Mobile laser (Opotek, Inc., Carlsbad, CA, USA) was tuned to 750 nm. Two types of fibers were connected to the laser system. The 1 mm-diameter optical fiber emitted an average energy of 550 $\mu$J per pulse. Three 1 mm-diameter fibers of a 1-to-7 fan-out optical fiber bundle each emitted average energies of 257 $\mu$J, 348 $\mu$J, or 335 $\mu$J per pulse.

To obtain photoacoustic images with the flexible array on different curved surfaces, three hemispherical phantoms with radii of curvature of 81.3 mm, 63.6 mm, and 50.8 mm, were made using plastisol. For brevity, these three phantoms will be referred to as the large, medium, and small phantoms, respectively. A hollow channel was bored in each phantom to insert a needle housing the individual optical fiber at fixed depths of 40 mm, 50 mm, and 40 mm in large, medium, and small phantoms, respectively. The flexible array transducer was placed on the curved surface of the phantom for photoacoustic data acquisition. A photograph of this experimental setup is shown in Fig. 1(a). Ten photoacoustic images were acquired per phantom.

In comparison to a single target, multiple targets introduce additional information based on relative target location and enable verification of image formation and scan conversion algorithms. To include multiple targets in a single photoacoustic image, a fourth plastisol hemispherical phantom with 81.3 mm radius of curvature was constructed. This phantom contained three hollow channels at depths of 40 mm, 50 mm, and 60 mm from the flat surface of the hemispherical phantom and will be referred to as the multi-target phantom. A photograph of the experimental setup for this phantom is shown in Fig. 1(b). In particular, three of the seven optical fibers from the 1-to-7 fan-out fiber bundle were individually inserted into one of the three channels described above. The flexible array was placed on the curved surface. Ten photoacoustic images of this setup were acquired, taking care to ensure alignment of the fiber tips with the elevation plane of the transducer.

### B. Image reconstruction

To create photoacoustic images, we assumed complete contact between the transducer and the curved side of the hemispherical phantom and the radius of curvature known. Thus, the geometry of the flexible array transducer was derived based on the radius of curvature of each phantom. This is a reasonable assumption if a transducer is fixed on a curved body part and measurements of the curvature can be obtained prior to photoacoustic imaging.

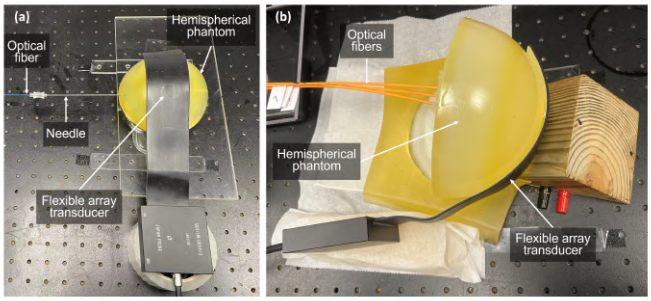


Fig. 1. Photographs of the experimental setups implemented to image the (a) single- and (b) multi-target phantoms

When implementing dynamic receive beamforming, the receive time delay varies at different depths. Unlike the linear array on a flat surface where all the element positions are fixed, the geometry of the flexible array changes according to the surface. Therefore, an angle $\theta$ was introduced to compute the $x$ and $z$ positions of each element. The time delay $\tau$ in dynamic receive delay-and-sum (DAS) beamforming with the flexible array was derived as follows:

$$\begin{aligned}\tau_i &= \frac{1}{c}[\sqrt{(R\sin\theta)^2 + (z_f - R + R\cos\theta)^2} - z_f] \\ &= \frac{1}{c}\left\{\sqrt{[R\sin(\frac{P_i}{R})]^2 + [z_f - R + R\cos(\frac{P_i}{R})]^2} - z_f\right\}\end{aligned} \tag{1}$$

where $c$ is the speed of sound, $z_f$ is the depth of the focal point, $R$ is the radius of curvature of the hemispherical phantom and the flexible array transducer, $P_i$ is the distance between the $i$th element and the element that is perpendicular to the focal point.

Digital scan conversion was then performed to convert the rectangular image into a sector photoacoustic image derived from the concave shape of the flexible transducer when placed on the hemispherical phantom surface.

### C. Image quality and target depth measurement

The size of the optical fiber tip in the scan-converted photoacoustic image was determined based on lateral and axial full-width at half-maximum (FWHM) measurements. Target visibility was determined with contrast and signal-to-noise ratio (SNR) measurements calculated as follows:

$$Contrast = 20\log_{10}\left(\frac{\mu_t}{\mu_b}\right) \tag{2}$$

$$SNR = 20\log_{10}\left(\frac{\mu_t}{\sigma_b}\right) \tag{3}$$

Authorized licensed use limited to: Johns Hopkins University. Downloaded on December 27,2022 at 04:18:09 UTC from IEEE Xplore. Restrictions apply.

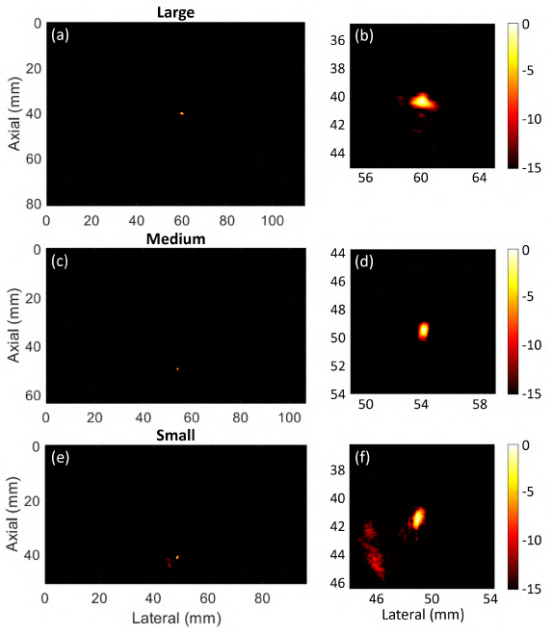


Fig. 2. Photoacoustic images and the 10 mm ×10 mm regions of interest (ROIs) surrounding targets within the (a,b) large phantom at 40 mm depth, (c,d) medium phantom at 50 mm depth, and (e,f) small phantom at 40 mm depth.

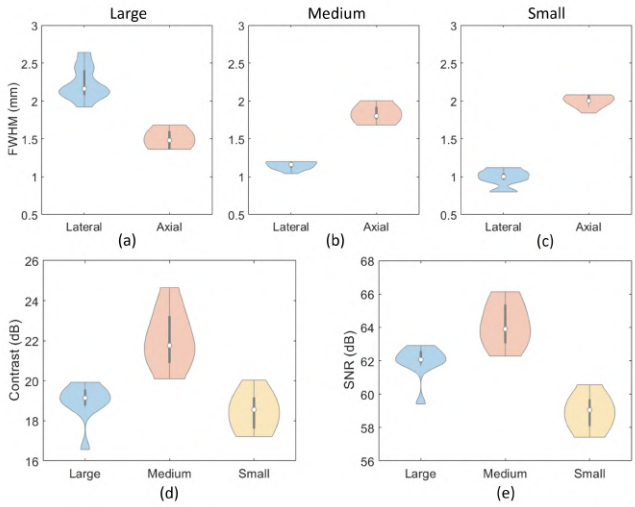


Fig. 3. Violin plots demonstrating target sizes measured in each image acquired with the (a) large, (b) medium, and (c) small phantoms (based on the lateral and axial FWHMs) and the target visibility based on (d) contrast and (e) SNR measurements.

where $\mu_t$ and $\mu_b$ are the means of the signal amplitude within target and background areas, which are square regions of interest (ROIs) inside and outside (i.e., at the same depth) of a photoacoustic target, respectively, and $\sigma_b$ is the standard deviation of amplitude within the background ROI.

Target was determined by the depth of the brightest pixel within the target ROI. To determine this target depth agreement with the ground truth (i.e., known fiber tip depth based on the phantom design), depth accuracy was defined as:

$$Accuracy = (1 - \frac{|D_t - D_g|}{D_g}) \times 100\% \quad (4)$$

where $D_t$ and $D_g$ are the depths of photoacoustic point target and ground truth.

## III. Results

Fig. 2 shows example photoacoustic images with the 1 mm-diameter optical fiber at depths of 40 mm, 50 mm, and 40 mm in the large, medium, and small phantoms, respectively. The mean target depths associated with the brightest point across all 10 images for the three phantom experiments were 40.46 mm, 49.40 mm, and 41.09 mm, and the depth agreements with the ground truths were 98.85%, 98.80%, and 97.28%, respectively.

Fig. 3 quantifies target size and target visibility measurements in violin plots, where the white circles denote medians and the colored shapes indicate data distributions. The ground truth is 1 mm in both lateral and axial dimensions as a 1 mm-diameter optical fiber was inserted. The median lateral and axial sizes assessed with the large, medium, and small phantoms are 2.16 mm and 1.48 mm, 1.16 mm and 1.80 mm, and 1.00 mm and 2.00 mm, respectively, as shown in Figs. 3(a-c). However, there are differences between the measured sizes and the ground truth. The maximum deviation of the target size from the ground truth is 1.6 mm, which is measured along the lateral axis in the large phantom. Figs. 3(d,e) show that contrast and SNR range 16.57 - 24.65 dB and 57.41 - 66.13 dB, respectively, across all phantom images, indicating good target visibility in each case.

Fig. 4(a) shows an example photoacoustic image of targets within the multi-target phantom. The mean target depths were 40.37 mm, 50.38 mm, and 59.01 mm for the 40 mm, 50 mm, and 60 mm target depths, respectively, corresponding to 99.08%, 99.24%, and 98.35% depth agreement, respectively.

Fig. 5(a) shows violin plots of measured target sizes. The median lateral and axial sizes are 1.12 mm and 1.60 mm, 1.16 mm and 1.36 mm, and 1.12 mm and 1.92 mm, for targets 1, 2, and 3, respectively. The maximum target size deviation from the ground truth is 1.2 mm. The mean ± standard deviation of combined target size measurements for single and multiple targets are 1.31 ± 0.12 mm in lateral dimension and 1.70 ± 0.11 mm in axial dimension.

Figs. 5(b) and 5(c) show contrast ranging 13.87 - 24.42 dB and SNR ranging 56.83 - 67.51 dB, indicating good target visibility. The mean ± standard deviation of contrast and SNR measurements in single and multi-target experiments combined are 19.05 ± 1.47 dB and 61.49 ± 1.47 dB, respectively.

## IV. Discussion and Conclusions

This paper presents the first known demonstration of photoacoustic imaging with a flexible array transducer in concave shapes for potential interventional applications. Photoacoustic images containing single and multiple targets were successfully reconstructed with the flexible array being placed on

Authorized licensed use limited to: Johns Hopkins University. Downloaded on December 27,2022 at 04:18:09 UTC from IEEE Xplore. Restrictions apply.

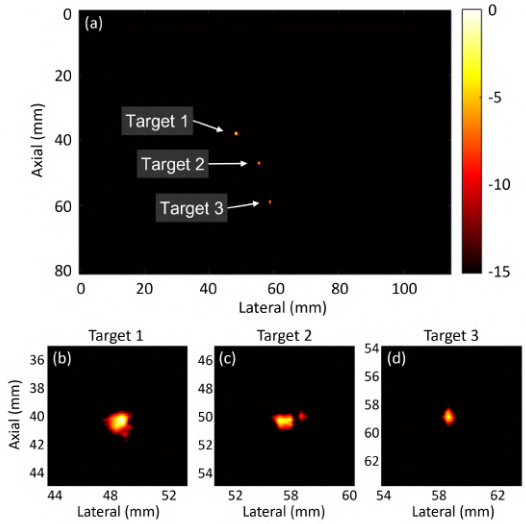


Fig. 4. Photoacoustic images of (a) three targets located at 40 mm, 50 mm, and 60 mm depths in the multi-target phantom and corresponding 10 mm $\times$10 mm ROIs surrounding (b) Target 1, (c) Target 2, and (d) Target 3.

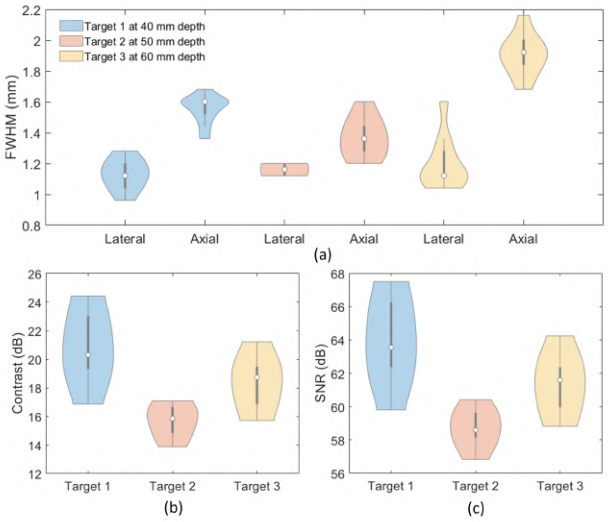


Fig. 5. Violin plots demonstrating (a) the measured size of the three targets located in the multi-target phantom and the target visibility in terms of (b) contrast and (c) SNR.

surfaces with three radii of curvature (i.e., 81.3 mm, 63.6 mm, 50.8 mm), 97.28 - 99.24% depth agreement compared to ground truth, $1.31 \pm 0.12$ mm lateral and $1.70 \pm 0.11$ mm axial target size, and $19.05 \pm 1.47$ dB contrast and $61.49 \pm 1.47$ dB SNR for target visibility. Possible reasons for the deviation of measured target size from the ground truth in single and multi-target experiments are that (1) the imaging plane might not be perpendicular to the fiber, (2) the fiber surface might be uneven, and (3) the signal measured in Fig. 3 might incorporate the metal needle surrounding the optical fiber. This work establishes the feasibility of a flexible array transducer for photoacoustic-guided surgery applications.

## REFERENCES


[1] M. Xu and L. V. Wang, "Photoacoustic imaging in biomedicine," *Review of Scientific Instruments*, vol. 77, no. 4, p. 041101, 2006.

[2] P. Beard, "Biomedical photoacoustic imaging," *Interface Focus*, vol. 1, no. 4, pp. 602–631, 2011.

[3] A. Wiacek and M. A. L. Bell, "Photoacoustic-guided surgery from head to toe," *Biomedical Optics Express*, vol. 12, no. 4, pp. 2079–2117, 2021.

[4] M. A. Lediju Bell, "Photoacoustic imaging for surgical guidance: Principles, applications, and outlook," *Journal of Applied Physics*, vol. 128, no. 6, p. 060904, 2020.

[5] J. Shubert and M. A. L. Bell, "Photoacoustic based visual servoing of needle tips to improve biopsy on obese patients," in *2017 IEEE International Ultrasonics Symposium (IUS)*, pp. 1–4, IEEE, 2017.

[6] M. Graham, F. Assis, D. Allman, A. Wiacek, E. Gonzalez, M. Gubbi, J. Dong, H. Hou, S. Beck, J. Chrispin, and M. A. L. Bell, "In vivo demonstration of photoacoustic image guidance and robotic visual servoing for cardiac catheter-based interventions," *IEEE Transactions on Medical Imaging*, vol. 39, no. 4, pp. 1015–1029, 2019.

[7] B. Eddins and M. A. L. Bell, "Design of a multifiber light delivery system for photoacoustic-guided surgery," *Journal of Biomedical Optics*, vol. 22, no. 4, p. 041011, 2017.

[8] J. Shubert and M. A. L. Bell, "A novel drill design for photoacoustic guided surgeries," in *Photons Plus Ultrasound: Imaging and Sensing 2018*, vol. 10494, pp. 38–43, SPIE, 2018.

[9] M. Blaivas, M. Lyon, L. Brannam, S. Duggal, and P. Sierzenski, "Water bath evaluation technique for emergency ultrasound of painful superficial structures," *The American Journal of Emergency Medicine*, vol. 22, no. 7, pp. 589–593, 2004.

[10] K. Nakahata, S. Tokumasu, A. Sakai, Y. Iwata, K. Ohira, and Y. Ogura, "Ultrasonic imaging using signal post-processing for a flexible array transducer," *NDT & E International*, vol. 82, pp. 13–25, 2016.

[11] M. T. Graham, J. Huang, F. X. Creighton, and M. A. L. Bell, "Simulations and human cadaver head studies to identify optimal acoustic receiver locations for minimally invasive photoacoustic-guided neurosurgery," *Photoacoustics*, vol. 19, p. 100183, 2020.

[12] J. Shubert and M. A. L. Bell, "Photoacoustic imaging of a human vertebra: implications for guiding spinal fusion surgeries," *Physics in Medicine & Biology*, vol. 63, no. 14, p. 144001, 2018.

[13] E. A. Gonzalez, A. Jain, and M. A. L. Bell, "Combined ultrasound and photoacoustic image guidance of spinal pedicle cannulation demonstrated with intact ex vivo specimens," *IEEE Transactions on Biomedical Engineering*, vol. 68, no. 8, pp. 2479–2489, 2020.

[14] K. M. Kempski, A. Wiacek, M. Graham, E. González, B. Goodson, D. Allman, J. E. Palmer, H. Hou, S. Beck, J. He, and M. A. L. Bell, "In vivo photoacoustic imaging of major blood vessels in the pancreas and liver during surgery," *Journal of Biomedical Optics*, vol. 24, no. 12, p. 121905, 2019.

[15] C. J. Lane, "The inspection of curved components using flexible ultrasonic arrays and shape sensing fibres," *Case Studies in Nondestructive Testing and Evaluation*, vol. 1, pp. 13–18, 2014.

[16] J. Chang, Z. Chen, Y. Huang, Y. Li, X. Zeng, and C. Lu, "Flexible ultrasonic array for breast-cancer diagnosis based on a self-shape–estimation algorithm," *Ultrasonics*, vol. 108, p. 106199, 2020.

[17] T. Noda, N. Tomii, K. Nakagawa, T. Azuma, and I. Sakuma, "Shape estimation algorithm for ultrasound imaging by flexible array transducer," *IEEE Transactions on Ultrasonics, Ferroelectrics, and Frequency Control*, vol. 67, no. 11, pp. 2345–2353, 2020.

[18] X. Huang, M. A. L. Bell, and K. Ding, "Deep learning for ultrasound beamforming in flexible array transducer," *IEEE Transactions on Medical Imaging*, vol. 40, no. 11, pp. 3178–3189, 2021.

[19] Q. T. K. Shea, Y. T. Ling, T. T.-Y. Lee, and Y. P. Zheng, "Spinal deformity measurement using a low-density flexible array ultrasound transducer: A feasibility study with phantoms," *Medicine in Novel Technology and Devices*, vol. 11, p. 100090, 2021.

[20] K. Roy, S. Agrawal, A. Dangi, T. Liu, H. Chen, T. N. Jackson, R. Pratap, and S.-R. Kothapalli, "Body conformal linear ultrasound array for combined ultrasound and photoacoustic imaging," in *2020 IEEE International Ultrasonics Symposium (IUS)*, pp. 1–4, IEEE, 2020.

[21] M. Ghavami, A. K. Ilkhechi, and R. Zemp, "Flexible transparent CMUT arrays for photoacoustic tomography," *Optics Express*, vol. 30, no. 10, pp. 15877–15894, 2022.


Authorized licensed use limited to: Johns Hopkins University. Downloaded on December 27,2022 at 04:18:09 UTC from IEEE Xplore. Restrictions apply.